Identifying the Origin of Finger Vein Samples Using Texture Descriptors

Babak Maser(✉) and Andreas Uhl

Multimedia Signal Processing and Security Lab, University of Salzburg, Salzburg, Austria
babak.maser@stud.sbg.ac.at, Uhl@cosy.sbg.ac.at

Abstract. Identifying the origin of a sample image in biometric systems can be beneficial for data authentication in case of attacks against the system and initiating sensor-specific processing pipelines in sensor-heterogeneous environments. Motivated by shortcomings of the photo response non-uniformity (PRNU) based method in the biometric context, we employ eight texture classification approaches, including frequency-, spatial-, and wavelet-based methods to detect finger vein samples images' origin. Besides, We use eight publicly available finger vein datasets and applying all eight novel classical texture descriptors and SVM classification in the suggested pipeline. A novel wavelet-based approach termed WMV demonstrated an excellent result for raw finger vein samples and the more challenging region of interest data among mentioned employed methods to identify sensor model. The observed results establish texture descriptors as effective competitors to PRNU in finger vein sensor model identification.

Keywords: Texture classification · Sensor identification · Image origin authentication · Finger vein recognition · PRNU · Texture descriptors

1 Introduction

Nowadays, we encounter a significant surge in the use of unattended applications of biometric systems. In many biometric modalities, a digital biometric image sensor is the core component for data acquisition, operating in the near-infrared (NIR) domain in the case of finger vein recognition. Identifying the origin of the query image is a vital task in digital image forensics. To establish the connection between a query image and the image's origin, we need to extract sensor information. Extraction of unique information of a biometric sensor can be done using various techniques and also at different levels. The aim is to extract the sensor information is to identify a sensor type and the technology used in the sensor or detect the sensor model and even the brand of the manufactured sensor. In biometrics, we also utilize the deduced information from the sensor to protect a recognition system against insertion attacks and enable the system to verify the ingenuity of image data samples. Independent biometric systems, the

© Springer Nature Switzerland AG 2021
O. Gervasi et al. (Eds.): ICCSA 2021, LNCS 12950, pp. 237–250, 2021.
https://doi.org/10.1007/978-3-030-86960-1_17

authenticity, and integrity of collected biometric data are critical to a biometric system's general stability and security issue. Attackers and Intruders always try to challenge the stability of the system. Considering an end-to-end biometric system, the Presentation Attack (PA) presents the spoofed artifacts to the sensor in contrast to the PA, Insertion Attack (IA) access directly to the feature extraction module. The feature extraction process can be done easily using another sensor, and to organize an insertion attack, the mentioned extracted information can be presented to a different biometric sensor or other modules of the recognition system. Obviously, the entire process of deducing information is done off-site. In the case of PA, the image can be manipulated to spoof the biometric system. In some complicated and advanced recognition systems, different sensors are presented. Each one may have different manufacturers or technology and models. In this complicated scenario, the interoperability of sensors is an important matter that can be impacted by how acquisition and image processing occurs on an in-sensor. Therefore, deducing sensors information leads us to utilize sensor specs to help and improve interoperability among the elements of recognition systems. And ultimately apply a sensor-tailored toolchain in a biometric system. Our work and research emphasize the feasibility of deducing sensor information in selective processing of the images and identifying the sensor model in a biometric recognition system, specifically for a finger vein (FV) sensor. We investigate the quality of captured finger vein data sample images using texture-based methods. There is a wide range of approaches to link the image's origin to the query image. One of the main approaches is exploiting the photo response non-uniformity (PRNU) [1]. However, the application of PRNU-based techniques in biometric sample data authentication has exhibited some difficulties: First, by analogy to the classical case, the PRNU fingerprint can be extracted from images of a biometric sensor and injected into forged sample images [2]. Only under certain restrictive conditions on available data can such attacks be detected or avoided (e.g., by applying the triangle test [3]). Second, authentication results with respect to biometric sensors have been reported to be widely varying at best (see e.g. [2,4,5] for iris sensor identification) and have been shown to be dependent and influenced by sensor components depicted in the images (see e.g. [6,7] for finger vein sensor identification). One reason for the difficulties is the requirement to compute the PRNU fingerprint from uncorrelated data - which is, of course, hard to satisfy given the high similarities among sample images present in biometric datasets [5,7]. Attempts to clarify this issue have not been convincing so far in the context of iris biometrics [8]. In finger vein biometrics, it has been shown that image content with a specifically structured characteristic and patterns (e.g., edge-like structures, finger positioning apparatus, illumination patterns) biases the estimated PRNU [7] as the extracted noise residual has to be independent of the image content. As a consequence, texture classification techniques have been proposed earlier to identify iris sensors at model level earlier [9,10]. However, contrasting to this present work, the authors of the former work propose rather costly techniques, i.e., improved Fisher vector encoding of denseSIFT and dense Micro-block difference features.

Therefore, due to the reasons explained, we launch a new investigation to examine the feasibility of identifying finger vein biometric sensors based on simple texture descriptors. In this work, we utilize classical descriptors, which are well known in computer vision, such as various wavelet-, frequency-, and spatial-based descriptors, respectively. Besides, we consider uncropped data samples (Original Samples), which exhibit highly correlated content, and we also study the effect in case sensor classification is done on regions of interest (ROIs) data, which do not depict special constant structures or patterns.

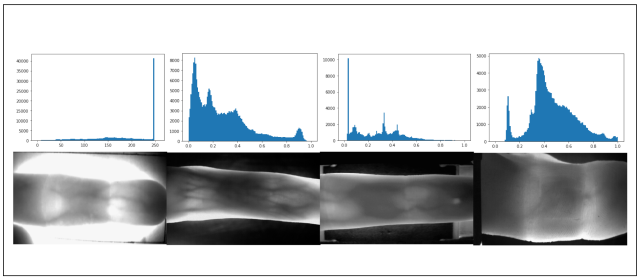

Fig. 1. Image and corresponding histogram samples of original sample images from left (a) HKPU_FV dataset, (b) UTFVP dataset, (c) SDUMLA dataset, and, (d) IDIAP dataset.

This work is structured as follows: In Sect. 2 we discuss the properties of the finger vein sample datasets as considered. Section 3 explains the conducted experiments in depth, where Subsect. 3.1 describes the used texture description methodology. Next, We discuss and analyze the experimental results in Sect. 4, and finally, we end this manuscript with a conclusion in Sect. 5.

2 Fingervein Sample Data

We considered eight different public finger vein datasets (acquired with distinct prototype near-infrared sensing devices), taking 120 samples from each dataset. As in finger vein recognition features are typically not extracted from a raw sample, but from a region-of-interest (ROI) image containing only finger vein texture, an insertion attack can also be mounted using such ROI data (in case the sensor does not deliver a raw sample to the recognition module but ROI data instead). Thus, we produced cropped ROI datasets out of the original ones (the description of the methodology is given afterward) to be able to test these data for their distinctiveness as well. Subsequently, we briefly detail the specifications of each dataset:

– **SDUMLA-HMT** [11]**:** Original resolution is 240×320, ROI data is 85×320 pixel. 120 images are selected from the first 30 subjects.

- **HKPU-FV** [12]**:** Original resolution is 256×513, ROI data is 60×390 pixel. 120 images are selected from the first 60 subjects.
- **IDIAP** [13]**:** Original resolution is 250×665, ROI data is 125×610 pixel. 120 images are selected from the first 60 subjects.
- **MMCBNU_6000 (MMCBNU)** [14]**:** Original resolution is 640×480, ROI data is 155×620 pixel. 120 images are selected from the first 20 subjects.
- **PLUS-FV3-Laser-Palmar (Palmar)** [15]**:** Original resolution is 600×1024, ROI data is 110×500 pixel. 120 images are selected from the first 20 subjects.
- **FV-USM** [16]**:** Original resolution is 480×640 pixels, ROI data is 110×280 pixel. 120 images are selected from the first 30 subjects.
- **THU-FVFDT** [15]**:** Original resolution is 600×1024, ROI data is 120×390 pixel. 120 images are selected from the first 120 subjects.
- **UTFVP** [17]**:** Original resolution is 380×672, ROI data is 140×490 pixel. 120 images are selected from the first 60 subjects.

Original sample images, as shown in Fig. 1, can be discriminated easily: Besides the differences in size (which can be adjusted by an attacker, of course), the sample images can probably be distinguished by the extent and luminance of the background. To illustrate this, we display the images' histograms above each example in Fig. 1, and those histograms clearly exhibit a very different structure. Thus, we expect texture descriptors to have an easy job of identifying the origin of the respective original sample images. The reason to use 120 images per dataset is to create the same environment and condition to have a comparable result to the PRNU-based investigations on these data (see [18]).

2.1 Generating Region of Interest Datasets

In finger vein recognition, contrasting to, e.g., fingerprint recognition, feature extraction is not applied to the entire raw sample data but instead to an ROI only [12,15]. In this ROI, only actual finger texture is contained. Depending on the setup of the system, the sensor might already extract the ROI from the raw sample. In this setting, identification of the finger vein data's origin has to be based on the ROI. Thus, it will be required under these circumstances that only finger vein texture (the ROI) is used to discriminate sensors. This is not unrealistic, as in the iris recognition case, normalized iris texture has been considered by analogy to be used for sensor identification [9,10] instead of raw iris sample data.

Different techniques have been applied to each dataset's properties to detect and segregate the finger vein region and extract a patch consisting of biometric data. For the datasets exhibiting a higher intra-variance of finger positions, we applied the following algorithm based on morphological snakes (morphological active contour without edges [19]) to extract the ROI (FV_USM, THU_FVDT, UTFVP, and MMCBNC datasets), also illustrated in Fig. 2:

1. Apply morphological snakes to the finger vein image to produce a segmented image.

2. Apply Canny edge detection and contour closing to detect the finger vein region.
3. Fill the contour.
4. Find the mass center of the filled contour and fit a line to the contour; estimate the angle (θ) of the line to the x-axis.
5. Rotate the texture area by θ degree.
6. Find the new mass center and crop the aligned original sample image.

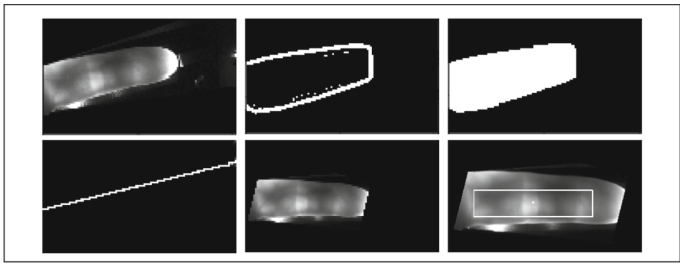

Fig. 2. ROI generation for datasets with finger position variability.

We also used this method for the Palmar dataset but replaced the morphological snakes' technique with the Chan-Vese segmentation algorithm [20].

To create the ROI for the (more straightforward) datasets HK_FV, IDIAP, and SDUMLA, we applied the following steps:

1. Apply Canny edge detection.
2. Apply a dilation operator on the detected edges.
3. Stack all images of a dataset on top of each other.
4. Fitting and cropping a rectangular (ROI) manually inside the finger vein area.

Figure 5 illustrates the results of ROI creation for a sample of each dataset (sample width has been normalized for better clarity). It gets immediately clear that discrimination is obviously more difficult based on the ROI data only. To investigate the differences between raw sample data and ROI data in more detail, we have investigated the range of luminance values and their variance across all datasets. Figures 3 and 4 display the results in the form of box-plots, where the left box-plot corresponds to the original raw sample data, and the right one to the ROI data, respectively. We can clearly see that the luminance distribution properties have been changed dramatically once we change our focus from original datasets to ROI datasets. For example, original HKPU_FV samples can be discriminated from FV_USM, MMCBNUm, PALMAR, UTFVP, and THU_FVFDT ones by just considering luminance value distribution. For the ROI data, the differences are not very pronounced anymore. When looking at the variance value distributions, we observe no such substantial discrepancy between the original

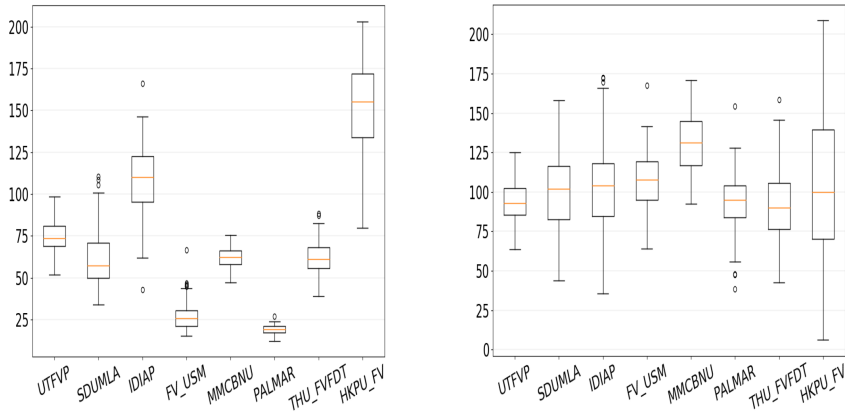

Fig. 3. Luminance distribution of original and ROI images across all datasets, respectively.

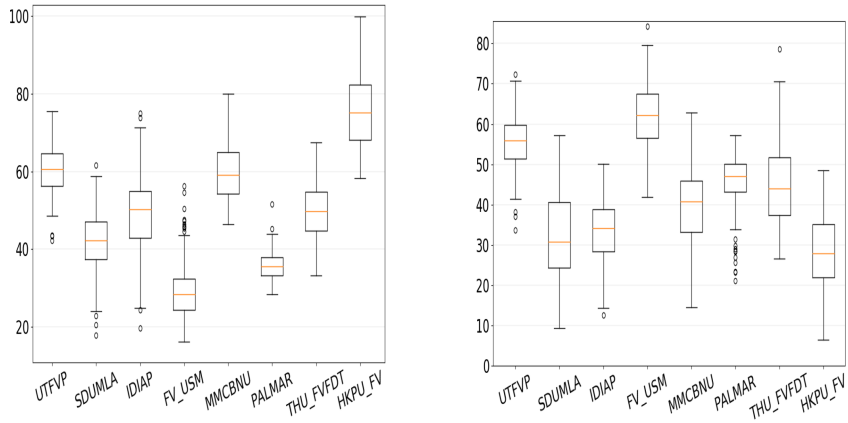

Fig. 4. Variance distribution of original and ROI images across all datasets, respectively.

sample and ROI data, still for some datasets, variance can be used as a discrimination criterion (e.g., Palmar vs. HKPU_FV in original data, FV_USM vs. HKPU_FV in ROI data). Consequently, we expect the discrimination of the considered datasets based on texture descriptors to be much more challenging when focusing on the ROI data only.

The steps to produce the cropping images is shown in Fig. 2. The size of cropped images for each dataset has been given in the Subsect. 2.

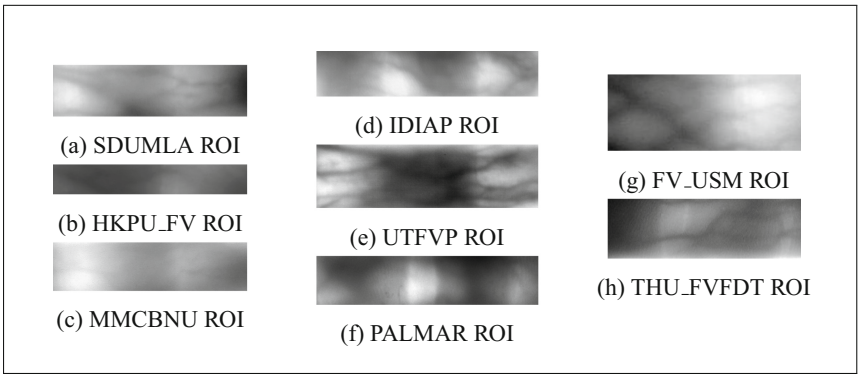

Fig. 5. ROI Samples from different datasets

3 Experimental Design

3.1 Texture Description Methodology

To discriminate sensors, we applied a number of classical yet simple approaches to produce a texture descriptor of a finger vein image. In the following subsections, we briefly describe the chosen techniques and explain how to cope with differently sized images.

Fourier Ring Filter (FRF). We generate features in the frequency domain using 2-D FFT. Independent of image size, fifteen bandpass filters split the frequency domain into equally sized bands, which are used to compute the mean and standard deviation of each ring [21] (which are used as statistical texture descriptors).

Local Binary Patterns (LBP). We use a variant of the original **Local Binary Pattern (LBP)** introduced by Ojala *et al.* [22]. This approach is called Histogram-LBP (HLBP [23]), we set the radius to 3, and the number of curricular neighborhood pixels is set to 15. The HLBP is invariant to image size if the output of the histogram for each image is normalized. Further, the number of histogram bins is fixed.

Additionally, we apply uniform LBP (ULBP) - an LBP is called uniform if the binary pattern contains at most two 0-1 or 1-0 transitions, and it has been shown that these patterns occur more frequently in natural texture (and significantly reduces feature-length vectors as the LBP histogram bins are reduced).

Image Histogram (IMHIST). We compute the image histogram and take the output as a feature vector. The IMHIST is invariant to image size by bin entry normalization and fixing the number of histogram bins.

Wavelet-Based Features. We apply 2-D wavelet decomposition using Daubechies 8-tap orthogonal filters to generate the coefficients in horizontal h, vertical v, and diagonal d directions. On every decomposition level, we compute the mean (μ) and standard deviation (std) for each of the sub-bands v, h, and d and concatenate those to get the mean and variance feature (WMV). We achieved invariance to image size by fixing the number of wavelet decomposition levels to 3.

Like WMV, we define wavelet variance (WV) by computing the variance per subband, and wavelet entropy (WE) by computing entropy per subband, respectively.

Local Entropy (LE). We slice a given image into 16 blocks (tiles) and compute the entropy from each tile. By taking a histogram of all produced entropies, a feature vector is generated. LE also is invariant to image size by fixing the number of image blocks (tiles) and bin number of the histogram.

3.2 SVM Finger Vein Texture Classification (FVTC)

The SVM classifier is trained by feeding 67% of all images then the remaining images 33% are used for the testing purpose. Images in all finger vein datasets are randomly shuffled beforehand to avoid subject-related bias. To optimize the SVM classifier and obtain the most promising hyperparameters such as C, γ, *kernel*, and *degree*, we employed a Grid Search technique with 4-fold cross-validation [24]. Also, we set the decision function to "*one vs rest*" strategy.

3.3 Evaluation Metrics

We use classical measures to rate our sensor identification task, which is a multi-class classification problem. The multi-class problem is an extension of binary classification. We use two evaluation approaches: First, receiver operating characteristic (ROC) which relates the false positive rate to the false negative rate, and second, the relation of precision and recall. For both relations, the Area Under The Curve (AUC) can be computed as a single measure.

Once we have multi-class problem, the challenging point is how to get an overall score. Often, one simply takes the average of the AUC-ROC metrics. For illustration, to calculate Recall for three-class problems, we sum up three Recalls and divide them by number of contributing classes, that is classical average. In contrast, another approach is based on summing up individual terms during the computation. In this work we obtained average of measurement metrics globally as shown in Eq. (1) and (2) (see [25,26]).

$$Avg\ Precision = \frac{\sum_c TP_c}{\sum_c TP_c + \sum_c FP_c} \tag{1}$$

$$Avg\ Recall = \frac{\sum_c TP_c}{\sum_c TP_c + \sum_c FN_c} \tag{2}$$

Where c is the class label, TP is True Positive, FN is False Negative and FP is False Positive.

3.4 Enhancement Techniques

To investigate the impact of enhancement on sensor identification we have decided to apply an enhancement method on uncropped datasets as well as ROI datasets. we applied the following methods.

1. **Wiener Filter and CLAHE (Enh.):** To enhance the quality of the images and remove undesired noise-related artifacts, we apply a Wiener Filter [27] and also to improve the contrast of images, and we use CLAHE (Contrast Limited Adaptive Histogram Equalization). Applying these two filters is done sequentially on all images of the mentioned datasets.
2. **No Enhancement (NoEnh.):** Sample images are used as present in the datasets or as obtained after ROI computation.

4 Result Analysis

Table 1 displays the experimental results. As expected, sensor identification is easily achieved based on original samples. Image enhancement improves results (mostly slightly) in many cases. We get values >0.99 in terms of AUC-ROC and AUC Precision-Recall for ULBP and WMV for both enhancement settings, which is a perfect result.

For ROI data, results deteriorate slightly. In particular, AUC Precision-Recall for spatial domain techniques is no longer acceptable. DFT and wavelet-based descriptors, however, still result in values well above 0.9, in most cases above 0.95, which is a very good result that could not be expected given the high similarity of textures and the simplicity of our descriptors. For ROI data, there is no clear trend if enhancement as being applied is beneficial or not. In any case, similar to the original sample case, for well-performing techniques, the difference is negligible.

Tables 2, 3, 4, 5, 6, 7, and 9 show the detailed outcomes of the proposed methodology for each sensor. In the mentioned tables, all of the Avg AUC-ROC scores for uncropped images are excellent, i.e., many results give an excellent Avg AUC-ROC score of 1.0. This implies that our approach may be considered as the best choice of image' origin identification (and is a hard competitor for the PRNU-based method when it comes to sensor model identification). As is expected from the overall results, also the estimated scores for uncropped images (ROI) are excellent, at least for the best methods considered. For those, the difference in result accuracy to original samples usually is seen only at the second precision digit after the decimal point.

When explicitly comparing our best result (i.e., AUC-ROC of the WMV descriptor of 0.999 and 0.994 for original and ROI samples, respectively) to the best PRNU results shown in [18] (Table 10), We notice the original Sample's superior value and compatible value on the ROI samples for the approach suggested in this work.

Table 1. Sensor identification results.

	Descriptor	Original sample		ROI	
		No.Enh	Enh.	No.Enh	Enh.
Avg AUC-ROC	FRF	0.997	0.999	0.989	0.986
Avg AUC Precision-Recall		0.987	0.999	0.952	0.932
Avg AUC-ROC	HLBP	0.992	0.994	0.941	0.955
Avg AUC Precision-Recall		0.960	0.968	0.762	0.783
Avg AUC-ROC	ULBP	0.995	0.999	0.931	0.932
Avg AUC Precision-Recall		0.994	0.997	0.763	0.728
Avg AUC-ROC	LE	0.919	0.952	0.834	0.858
Avg AUC Precision-Recall		0.685	0.772	0.538	0.650
Avg AUC-ROC	ImHist	0.989	0.961	0.906	0.966
Avg AUC Precision-Recall		0.883	0.789	0.481	0.851
Avg AUC-ROC	WV	0.998	0.998	0.984	0.983
Avg AUC Precision-Recall		0.991	0.994	0.930	0.909
Avg AUC-ROC	WE	0.993	0.985	0.977	0.959
Avg AUC Precision-Recall		0.979	0.943	0.902	0.854
Avg AUC-ROC	WMV	0.999	0.999	0.982	0.994
Avg AUC Precision-Recall		0.999	0.996	0.917	0.971

Table 2. FRF exhibits how well detects and identifies different sensors, the mentioned values are Avg AUC-ROC scores

Sensor	Uncropped image		ROI	
	No.Enh	Enh.	No.Enh	Enh.
UTFVP	1.000	1.000	0.971	0.951
FV_USM	1.000	1.000	0.983	0.955
PALMAR	0.999	1.000	0.988	0.975
SDUMLA	0.988	1.000	1.000	1.000
THU_FVFDT	1.000	1.000	1.000	1.000
IDIAP	1.000	1.000	1.000	1.000
MMCBNU	0.992	0.999	0.961	0.968
HKPU-FV	1.000	1.000	1.000	1.000

Table 3. Wavelet Variance exhibits how well detects a identifies different sensors, the mentioned values are Avg AUC-ROC scores

Sensor	Uncropped image		ROI	
	No.Enh	Enh.	No.Enh	Enh.
UTFVP	0.996	1.000	0.938	0.954
FV_USM	1.000	0.997	1.000	0.992
PALMAR	1.000	0.999	0.995	0.999
SDUMLA	1.000	1.000	1.000	0.995
THU_FVFDT	0.998	0.999	0.951	0.980
IDIAP	1.000	1.000	0.996	0.990
MMCBNU	1.000	1.000	0.955	0.944
HKPU-FV	1.000	1.000	0.996	0.975

Table 4. Wavelet mean Variance exhibits how well detects and identifies different sensors, the mentioned values are Avg AUC-ROC scores

Sensor	Uncropped image		ROI	
	No.Enh	Enh.	No.Enh	Enh.
UTFVP	1.000	1.000	0.930	0.993
FV_USM	1.000	1.000	0.998	0.997
PALMAR	1.000	0.999	0.995	0.997
SDUMLA	1.000	1.000	1.000	1.000
THU_FVFDT	0.999	0.999	0.983	0.994
IDIAP	1.000	1.000	0.990	0.992
MMCBNU	1.000	1.000	0.988	0.994
HKPU-FV	1.000	1.000	0.991	0.988

Table 5. Wavelet Entropy exhibits how well detects and identifies different sensors, the mentioned values are Avg AUC-ROC scores

Sensor	Uncropped image		ROI	
	No.Enh	Enh.	No.Enh	Enh.
UTFVP	0.996	0.9960	0.972	0.969
FV_USM	0.992	0.9460	0.992	0.967
PALMAR	0.970	0.9903	0.999	0.985
SDUMLA	0.997	0.9844	1.000	0.962
THU_FVFDT	1.000	1.0000	0.948	0.889
IDIAP	1.000	1.0000	0.977	0.951
MMCBNU	0.992	0.9493	0.922	0.935
HKPU-FV	1.000	0.9997	0.965	0.992

Table 6. Histogram LBP exhibits how well detects and identifies different sensors, the mentioned values are Avg AUC-ROC scores

Sensor	Uncropped image		ROI	
	No.Enh	Enh.	No.Enh	Enh.
UTFVP	0.998	0.994	0.937	0.922
FV_USM	0.954	0.954	0.910	0.917
PALMAR	0.997	0.999	0.870	0.925
SDUMLA	0.994	0.990	0.948	0.969
THU_FVFDT	0.985	0.996	0.977	0.969
IDIAP	0.999	1.000	0.988	0.996
MMCBNU	0.997	1.000	0.901	0.929
HKPU-FV	1.000	1.000	0.978	0.977

Table 7. Uniform LBP exhibits how well detects and identifies different sensors, the mentioned values are Avg AUC-ROC scores

Sensor	Uncropped image		ROI	
	No.Enh	Enh.	No.Enh	Enh.
UTFVP	0.988	0.994	0.918	0.952
FV_USM	0.999	0.999	0.978	0.950
PALMAR	1.000	1.000	0.896	0.827
SDUMLA	1.000	1.000	1.000	0.999
THU_FVFDT	1.000	1.000	0.839	0.866
IDIAP	1.000	1.000	0.955	0.935
MMCBNU	1.000	1.000	0.821	0.880
HKPU-FV	1.000	1.000	0.990	0.986

Table 8. Image Histogram (Im Hist) exhibits how well detects and identifies different sensors, the mentioned values are Avg AUC-ROC scores

Sensor	Uncropped image		ROI	
	No.Enh	Enh.	No.Enh	Enh.
UTFVP	1.000	0.999	0.934	0.932
FV_USM	0.977	0.991	0.916	0.935
PALMAR	0.999	0.933	0.654	0.987
SDUMLA	0.999	0.976	0.950	0.960
THU_FVFDT	1.000	1.000	0.989	1.000
IDIAP	1.000	1.000	0.975	0.999
MMCBNU	0.958	0.874	0.911	0.877
HKPU-FV	1.000	1.000	0.920	0.996

Table 9. Local Entropy (LE) exhibits how well detects and identifies different sensors, the mentioned values are Avg AUC-ROC scores

Sensor	Uncropped image		ROI	
	No.Enh	Enh.	No.Enh	Enh.
UTFVP	0.939	0.917	0.651	0.825
FV_USM	0.920	0.973	0.865	0.932
PALMAR	0.928	0.951	0.783	0.901
SDUMLA	0.867	0.890	0.990	0.999
THU_FVFDT	0.993	0.998	0.985	1.000
IDIAP	0.756	0.872	0.707	0.693
MMCBNU	0.973	0.973	0.737	0.261
HKPU-FV	0.950	0.963	0.611	0.806

Table 10. Comparing results of the PRNU and the Texture Descriptors approaches on the original and the ROI sample data.

	PRNU		Texture descriptors
	NCC	PCE	WMV
Original sample	0.992	0.991	0.999
ROI	0.998	0.997	0.994

5 Conclusion

We have identified texture descriptors as being well suited for finger vein sensor *model* identification, being applied to raw sample images as well as to the more challenging finger vein ROI data. Enhancement techniques turn out to be non-decisive for classification accuracy, at least when considering top-performing techniques. Overall, but especially when considering results for ROI data, frequency-based and wavelet-based descriptors are found to perform superior to spatial domain techniques. Specifically, We introduced a novel wavelet-based texture descriptor method termed WMV that demonstrated excel on various datasets. The excellent results suggest the proposed techniques be better suited as compared to PRNU-based methods for the task investigated. Also, a fusion of both approaches seems promising, which will be subject to further investigations.

References

1. Chen, M., Fridrich, J., Goljan, M., Lukás, J.: Determining image origin and integrity using sensor noise. IEEE Trans. Inf. Forensics Secur. **3**(1), 74–90 (2008)
2. Uhl, A., Höller, Y.: Iris-sensor authentication using camera PRNU fingerprints. In: Proceedings of the 5th IAPR/IEEE International Conference on Biometrics, ICB 2012, New Delhi, March 2012, India, pp. 1–8 (2012)
3. Goljan, M., Fridrich, J., Chen, M.: Sensor noise camera identification: countering counter-forensics. In: Media Forensics and Security II, vol. 7541, p. 75410S. International Society for Optics and Photonics (2010)
4. Kalka, N., Bartlow, N., Cukic, B., Ross, A.: A preliminary study on identifying sensors from iris images. In: Proceedings of the IEEE Conference on Computer Vision and Pattern Recognition Workshops, pp. 50–56 (2015)
5. Debiasi, L., Sun, Z., Uhl, A.: Generation of iris sensor PRNU fingerprints from uncorrelated data. In: Proceedings of the 2nd International Workshop on Biometrics and Forensics, IWBF 2014, Valletta, Malta, pp. 1–6 (2014)
6. Söllinger, D., Maser, B., Uhl, A.: PRNU-based finger vein sensor identification: on the effect of different sensor croppings. In: 2019 International Conference on Biometrics (ICB), pp. 1–8 (2019)

7. Söllinger, D., Debiasi, L., Uhl, A.: Can you really trust the sensor's PRNU? How image content might impact the finger vein sensor identification performance. In: Proceedings of the 25th International Conference on Pattern Recognition (ICPR), pp. 7782–7789 (2020)
8. Debiasi, L., Uhl, A.: Techniques for a forensic analysis of the CASIA-Iris V4 database. In: Proceedings of the 3rd International Workshop on Biometrics and Forensics, IWBF 2015, Gjovik, Norway, pp. 1–8 (2015)
9. Debiasi, L., Kauba, C., Uhl, A.: Identifying iris sensors from iris images. In: Iris and Periocular Biometric Recognition, vol. 5, p. 359 (2017)
10. El-Naggar, S., Ross, A.: Which dataset is this iris image from? In: 2015 IEEE International Workshop on Information Forensics and Security (WIFS), pp. 1–6. IEEE (2015)
11. Yin, Y., Liu, L., Sun, X.: SDUMLA-HMT: a multimodal biometric database. In: Sun, Z., Lai, J., Chen, X., Tan, T. (eds.) CCBR 2011. LNCS, vol. 7098, pp. 260–268. Springer, Heidelberg (2011). https://doi.org/10.1007/978-3-642-25449-9_33
12. Kumar, A., Zhou, Y.: Human identification using finger images. IEEE Trans. Image Process. **21**(4), 2228–2244 (2012)
13. Tome, P., Vanoni, M., Marcel, S.: On the vulnerability of finger vein recognition to spoofing. In: IEEE International Conference of the Biometrics Special Interest Group (BIOSIG) (September 2014)
14. Lu, Y., Xie, S.J., Yoon, S., Wang, Z., Park, D.S.: An available database for the research of finger vein recognition. In: 2013 6th International Congress on Image and Signal Processing (CISP), CISP 2013, vol. 1, pp. 410–415. IEEE (2013)
15. Kauba, C., Prommegger, B., Uhl, A.: Focussing the beam - a new laser illumination based data set providing insights to finger-vein recognition. In: Proceedings of the IEEE 9th International Conference on Biometrics: Theory, Applications, and Systems, BTAS 2018, Los Angeles, California, USA, pp. 1–9 (2018)
16. Asaari, M.S.M., Rosdi, B.A., Suandi, S.A.: Fusion of band limited phase only correlation and width centroid contour distance for finger based biometrics. Exp. Syst. Appl. **41**(7), 3367–3382 (2014)
17. Ton, B.T., Veldhuis, R.N.J.: A high quality finger vascular pattern dataset collected using acustom designed capturing device. In: International Conference on Biometrics, ICB 2013. IEEE (2013)
18. Söllinger, D., Maser, B., Uhl, A.: PRNU-based finger vein sensor identification: on the effect of different sensor croppings. In: 2019 International Conference on Biometrics (ICB), pp. 1–8. IEEE (2019)
19. Chan, T.F., Vese, L.A.: Active contours without edges. IEEE Trans. Image Process. **10**(2), 266–277 (2001)
20. Getreuer, P.: Chan-Vese segmentation. IPOL J. **2**, 214–224 (2012)
21. Vécsei, A., Fuhrmann, T., Liedlgruber, M., Brunauer, L., Payer, H., Uhl, A.: Automated classification of duodenal imagery in celiac disease using evolved Fourier feature vectors. Comput. Meth. Program. Biomed. **95**, S68–S78 (2009)
22. Ojala, T., Pietikäinen, M., Harwood, D.: A comparative study of texture measures with classification based on featured distributions. Pattern Recogn. **29**(1), 51–59 (1996)
23. Boulogne, F., Warner, J.D., Yager, E.N.: scikit-image: Image processing in Python. PerrJ **2**, e453 (2014)
24. Kohavi, R., et al.: A study of cross-validation and bootstrap for accuracy estimation and model selection. In: IJCAI, vol. 14, Montreal, Canada, pp. 1137–1145 (1995)

25. Ferri, C., Hernández-Orallo, J., Salido, M.A.: Volume under the ROC surface for multi-class problems. In: Lavrač, N., Gamberger, D., Blockeel, H., Todorovski, L. (eds.) ECML 2003. LNCS (LNAI), vol. 2837, pp. 108–120. Springer, Heidelberg (2003). https://doi.org/10.1007/978-3-540-39857-8_12
26. Van Asch, V.: Macro-and micro-averaged evaluation measures. In: CLiPS, Belgium, vol. 49 (2013)
27. Benesty, J., Chen, J., Huang, Y., Doclo, S.: Study of the wiener filter for noise reduction. In: Speech Enhancement. Signals and Communication Technology. Springer, Heidelberg (2005). https://doi.org/10.1007/3-540-27489-8_2